Characterization of hydrogen traps in a co-precipitation steel investigated by atom probe experiments without cryogenic transfer

Scripta Materialia 243 (2024) 115963

Contents lists available at ScienceDirect

Scripta Materialia

journal homepage: www.journals.elsevier.com/scripta-materialia

Characterization of hydrogen traps in a co-precipitation steel investigated by atom probe experiments without cryogenic transfer

Severin Jakob [a,*], Mohammad Sattari [a], Birhan Sefer [b], Steve Ooi [c,d], Mattias Thuvander [a,*]

[a] Department of Physics, Chalmers University of Technology, Göteborg SE-412 96, Sweden
[b] Group of Corrosion and Hydrogen Embrittlement, Materials Development Department, Swerim AB, Box 7047, Kista 164 07, Sweden
[c] Maxwell Centre, Ovako Group R&D, JJ Thompson Avenue, Cambridge CB3 0HE, United Kingdom
[d] Ovako Corporate R&D, Building 202, Hofors SE-813 82, Sweden

ARTICLE INFO

Keywords:
Atom probe tomography
Co-precipitation
Hydrogen trapping

ABSTRACT

Hydrogen (H) embrittlement in high-strength steels can be mitigated by introducing H traps into the microstructure. The co-precipitation model steel in this work contains intermetallic ß-NiAl and secondary Cr-carbides, which provide abundant trapping sites. Needle-shaped specimens are prepared for atom probe tomography (APT) and electro-chemically charged in a solution of 0.1 M NaOH in D_2O to introduce deuterium (D). D is located at the finely dispersed Cr-carbides even after specimen transfer at room temperature (RT), which shows that nano-sized Cr-carbides are strong H traps. This is in contrast to previous studies of weak traps where cryogenic transfer was needed to detect any D.

High-strength steels with improved mechanical properties are desired among other in lightweight design of structural components. With higher yield strength, smaller amounts of material are used in the same application, leading to reduced resource consumption and overall lower costs. However, high-strength steels are sensitive to hydrogen embrittlement (HE) due to the high stress concentration and the suppression of dislocation emission at the crack tip caused by accumulation of H [1–3]. It has been shown that a critical content of diffusible H leads to material failure [4].

The idea to prevent HE by trapping H in the microstructure is not new [5,6]. Grain boundaries and dislocations have been shown to only weakly trap H [3]. Therefore, other nanostructures in form of carbides, such as NbC, TiC, VC and Mo_2C, or ε-Cu precipitates were investigated as H traps [7–11]. The amount of trapped H and the strength of binding are usually measured by thermal desorption mass spectrometry (TDMS) [9,10]. More recently, investigations into the actual trapping sites were performed with APT instruments [12–15]. APT offers nearly atomic spatial resolution with high sensitivity for all elements [16]. However, quantitative characterization of H is still challenging. Since H_2 is the main residual gas in the ultra-high vacuum (UHV) chamber, the presence of H^+, or in addition H_2^+ depending on the measurement mode, ions in the mass spectrum is a common artefact during APT experiments [17]. A practical way to distinguish between H from the vacuum chamber and actual H in the material is the use of the heavier isotope deuterium. It was shown that D has similar solubility and only slightly lower diffusivity compared to H, making it suitable for this kind of experiments [18,19]. D is either introduced into the specimen by gas charging [12,13], implantation [20] or electro-chemically by cathodic charging of the specimen in D_2O solutions [15,21–23]. To prevent H or D from diffusing and escaping the material, the use of cryogenic transfer has been emphasized [24–26]. So far, D was hardly measured without fast cooling the specimen and maintaining a continuous cold transfer to the analysis chamber.

A promising material design concept for high strength and resistance to HE is known as dual-hardening steel [27–30]. The high mechanical strength, good fatigue resistance, and adequate deformability are achieved by precipitating two types of particles with high number densities in a martensitic matrix [27]. As shown for Hybrid steel® from Ovako AB, the improved strength is maintained at elevated temperatures due to the reduced coarsening of particles compared to other steels [30]. Similar to the development of Hybrid steel® [31], the model alloy in this paper was designed to have a lean alloying concept with balanced mechanical properties as well as a high resistance to HE. The Hybrid model alloy has two different types of particles, namely intermetallic ß-NiAl as well as secondary Cr-carbides. Samples are charged with D and moved to the APT instrument without cryogenic transfer. It is shown from the APT

* Corresponding authors.
E-mail addresses: severin.jakob@chalmers.se (S. Jakob), mattias.thuvander@chalmers.se (M. Thuvander).

https://doi.org/10.1016/j.scriptamat.2023.115963
Received 5 July 2023; Received in revised form 21 November 2023; Accepted 27 December 2023
Available online 5 January 2024

measurements that nano-scale Cr-carbides are strong traps for H since D is still present in the measurements even after RT transfer.

The Hybrid model alloy in this work (0.42 C, 6.5 Cr, 2.5 Al, 3 Ni and 0.25 Mo in wt.%) was solution annealed and quenched before aging for 20 h at 500 °C. The microstructure was characterized by scanning transmission electron microscopy (S/TEM), using an FEI Titan 80–300 TEM operating at 300 kV as well as APT. Thin foils were prepared by mechanically thinning a 3 mm disk to around 100 µm thickness, followed by electrolytic twin-jet polishing in 10 % perchloric acid solution cooled to -30 °C at 20 V. Samples for APT were cut to 0.3 × 0.3 × 15 mm^3 and needle-shaped specimens were prepared by a two-step electropolishing process in 10 % and 2 % perchloric acid, respectively [16].

APT specimens were characterized without charging as well as cathodically charged in a solution of 0.1 M NaOH in D_2O at -2.2 V against a Pt counter-electrode for 30 s. After charging, the specimen was mounted and moved through the load-lock and buffer chamber of the atom probe instrument. The transfer-time at RT was about 15 min before the APT needle was cooled to cryogenic temperature in the analysis chamber.

The specimens were measured on the latest generation of APT instruments, a LEAP 6000XR from CAMECA Instruments. This instrument is equipped with a reflectron and has a detection efficiency of 52 %. APT measurements were performed at 70 K in voltage mode with 20 % pulse fraction, 0.5 - 1 % detection rate and pulse frequencies of 100, 200 and 333 kHz. The reconstructions were made in the commercial software AP Suite 6.3 (CAMECA) using the voltage method with an image compression factor of 1.65 and a field factor of 4.0. The sizes of nano-scale precipitates were characterized by applying the parameter free method by Zhao et al. [32], which uses the radial distribution function. The matrix contents were determined by the DIAM method that is based on nearest neighbor distributions [33]. Particle sizes were calculated from the number of atoms, hence, avoiding local magnification effects [34,35].

To investigate the de-trapping activation energy, TDMS was conducted using a Bruker Galileo G8 analyzer in combination with a mass spectrometer from InProcess Instrument GmbH for H detection. Nitrogen was used as the carrier gas and pure hydrogen gas was used to calibrate the instrument. Samples with dimensions of 1 × 10 × 13 mm^3 were prepared with surface finish of P600 SiC sanding paper and charged in 3 wt.% NaCl and 0.3 wt.% NH_4SCN electrolyte at -1 mA/cm^2 for 24 h. After degassing for 24 h at 50 °C, one set of samples was measured with 0.3, 0.6 and 1.2 °C/s heating rates from RT to 800 °C. To investigate the degassing behavior, one sample was measured directly after cathodic charging and two more samples were degassed at 50 °C for 72 h and 168 h before TDMS analysis using 0.6 °C/s. Analysis of de-trapping activation energies is based on the formulation of Kissinger [36] and the simplified models thereof as shown by Lee and Lee [37] and Wei et al. [38].

Fig. 1(a) and 1(b) show TEM micrographs of the microstructure, showing martensite laths with particles of about 10 to 100 nm in size at the boundaries. The composition of the particles was measured with energy dispersive X-ray spectroscopy (EDX) and revealed on one hand Ni and Al in equal amounts and on the other hand Cr-carbides with C and Fe in different concentrations. The small size and hence contribution of the surrounding matrix to the EDX signal makes it difficult to measure the exact composition of the particles.

High resolution TEM was performed within the laths, showing smaller particles. The particle in Fig. 1(c) has about 4 nm width and shows an interplanar spacing of 2.06 Å. The closest match for this is $M_{23}C_6$ (511) planes (ICCD card number 01–078–1499) with $d = 2.05$ Å. However, M_7C_3 with 2.10 Å plane spacing of (202) planes (ICCD card number 04-005-9650) cannot be excluded as a possible crystal structure. Another particle, shown in Fig. 1(d), with an interplanar spacing of 1.97 Å can be best approximated by M_7C_3 (600) planes, having $d = 1.99$ Å

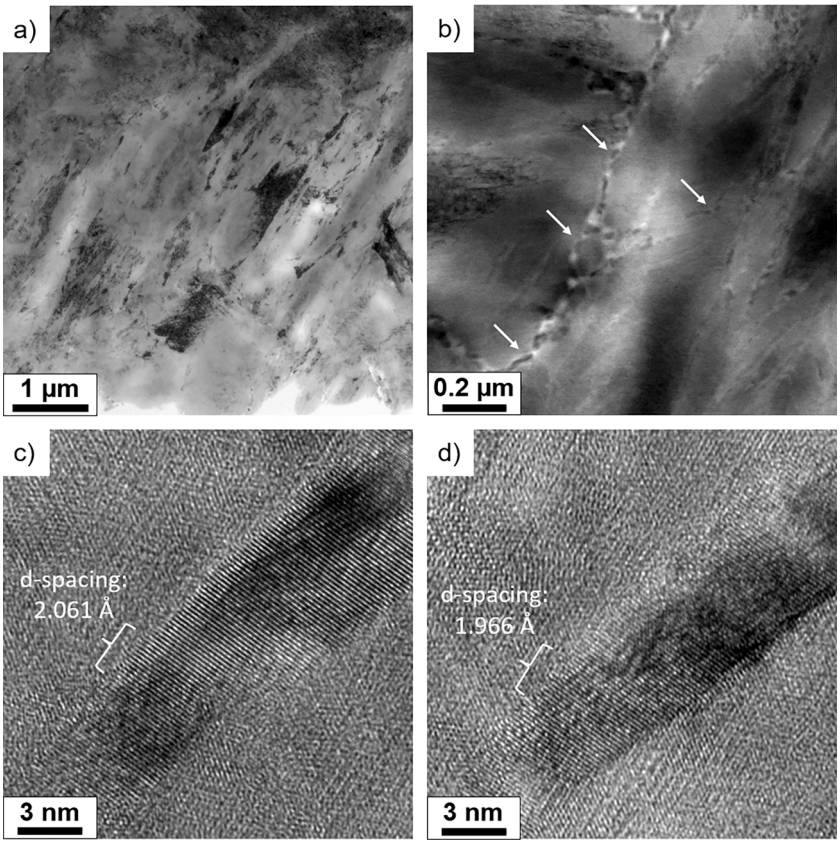

Fig. 1. (a–b) TEM micrographs showing the martensitic microstructure with particles at the lath boundaries (indicated by arrows). (c-d) show high resolution TEM of precipitates within the laths and their interplanar spacing.

(ICCD card number 04–005–9650).

Fig. 2(a) shows a 5 nm thick sections of an APT reconstruction of an uncharged specimen (overall 5.7 million ions collected). The elements, which are relevant for precipitation, are depicted. Iron, as the main element in the alloy, as well as some minor elements are not shown for visibility. The two different particle types can be clearly distinguished. On one hand, ß-NiAl with about a 1:1 ratio of Ni and Al atoms and about 20 at.% Fe forms spherical precipitates with an average diameter of 1.60 ± 0.11 nm. It has been shown that ß-NiAl incorporates Fe, especially during the early stages of precipitation [39]. On the other hand, Cr-carbide precipitates nucleate heterogeneously on ß-NiAl as well as on dislocations and grain/lath boundaries. Consequently, the particles are not spherical. The mean size, determined as average diameter, was calculated to be 2.15 ± 0.08 nm.

Fig. 2(b) shows the mass-spectrum of an uncharged specimen. The distinct peaks in this mass-to-charge range correspond to H^+ and C^{2+} ions. In comparison to that, the same mass-to-charge range of the mass-spectrum for the charged specimen is presented in Fig. 2(d). Besides the expected H^+ and C^{2+} peaks, a prominent peak at 2 Da corresponding to D^+ is present.

Fig. 2(c) shows a 5 nm thick section of the reconstruction of the charged specimen. Again, ß-NiAl as well as Cr-carbide precipitates are visible. In addition, the measured D ions are depicted as red spheres. The distribution of these ions seems to be closely connected to the Cr-carbides. Interestingly, ß-NiAl does not seem to attract and trap D.

To visualize and analyze particles, iso-concentration surfaces are widely used. Fig. 3(a) depicts the reconstruction of the charged specimen with 1 nm voxel size and 3 nm delocalization. The threshold for iso-concentration surfaces was set to 7 at.% Cr and the proximity histogram, also known as proxigram, is plotted in Fig. 3(b). The proxigram shows the composition as a function of distance to the iso-concentration surface. Within the Cr-carbide precipitates, Ni and Al are depleted, whereas Mo is enriched. The depiction of a sharp interface is limited by the lateral resolution of the APT measurement as well as local magnification effects between the different phases [34]. Hence, a significant proportion of Fe is recorded (not shown in Fig. 3) within the precipitates and the C content will not reach a stochiometric composition for carbides of this size. During characterization of uncharged specimens of this material, two populations of nano-scale carbides were apparent, similar to the slightly larger particles from the TEM investigation. Proxigrams of the different nano-scale precipitates in this material are shown in the supplementary material. Most carbides have a measured C content of about 16 at.%. Considering C loss from multiples, these carbides correspond to $M_{23}C_6$ [40]. The other carbide population has higher C and corresponds to M_7C_3. Fig. 3(c) displays the D, C and Cr contents. D is in very low concentration at distances far from the Cr-carbide precipitates. However, it is enriched in the region where C and Cr are starting to increase. Deuterium remains at an elevated concentration within the carbides. The error bars correspond to the counting statistics as computed by AP Suite and are higher deeper inside the carbides since fewer ions are sampled.

The charged specimen, shown in Fig. 2(c) was measured with three different voltage pulse frequencies to employ the evaporation rate method as demonstrated by Meier et al. [41]. The H content from the vacuum chamber is dependent on the time between evaporation events, as was previously shown by Sundell et al. [17]. By varying frequency and/or detection rate, the H content could be measured despite the presence of a contaminant H background signal. 1.1 million ions were collected with 200 kHz pulse frequency and 300 000 ions with 100 and 333 kHz each. The concentrations of H, D, and C are displayed in Fig. 4. The concentration of H clearly depends on the frequency and thus confirming the expected supply mechanism from the UHV chamber. In contrast, the D concentration does not correlate with the frequency. Rather, higher D content is seen in sections of the run with higher C

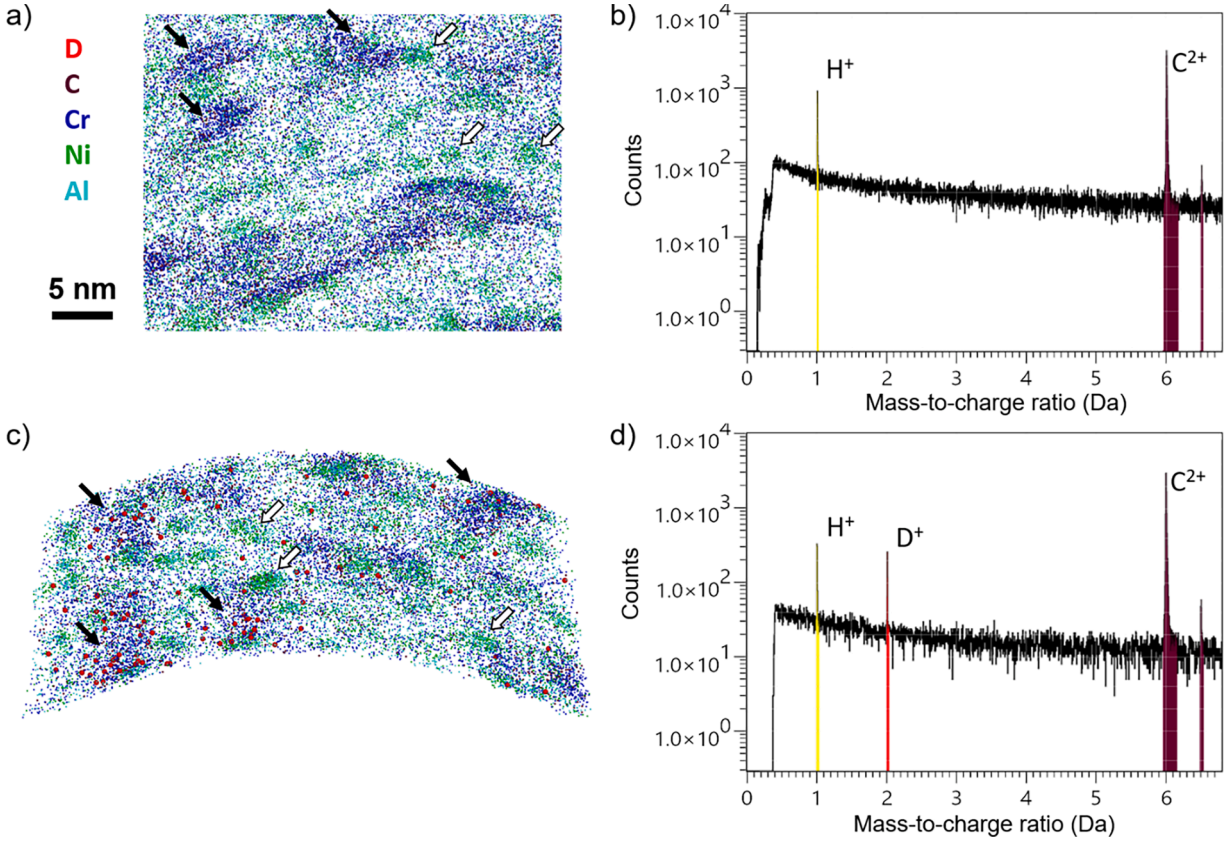

Fig. 2. Distribution of precipitation forming elements as well as D within a 5 nm thick section of APT reconstructions and selected mass-spectrum ranges of uncharged (a-b) and D charged (c-d) specimens. Solid arrows indicate exemplary carbides and open arrows show intermetallic particles.

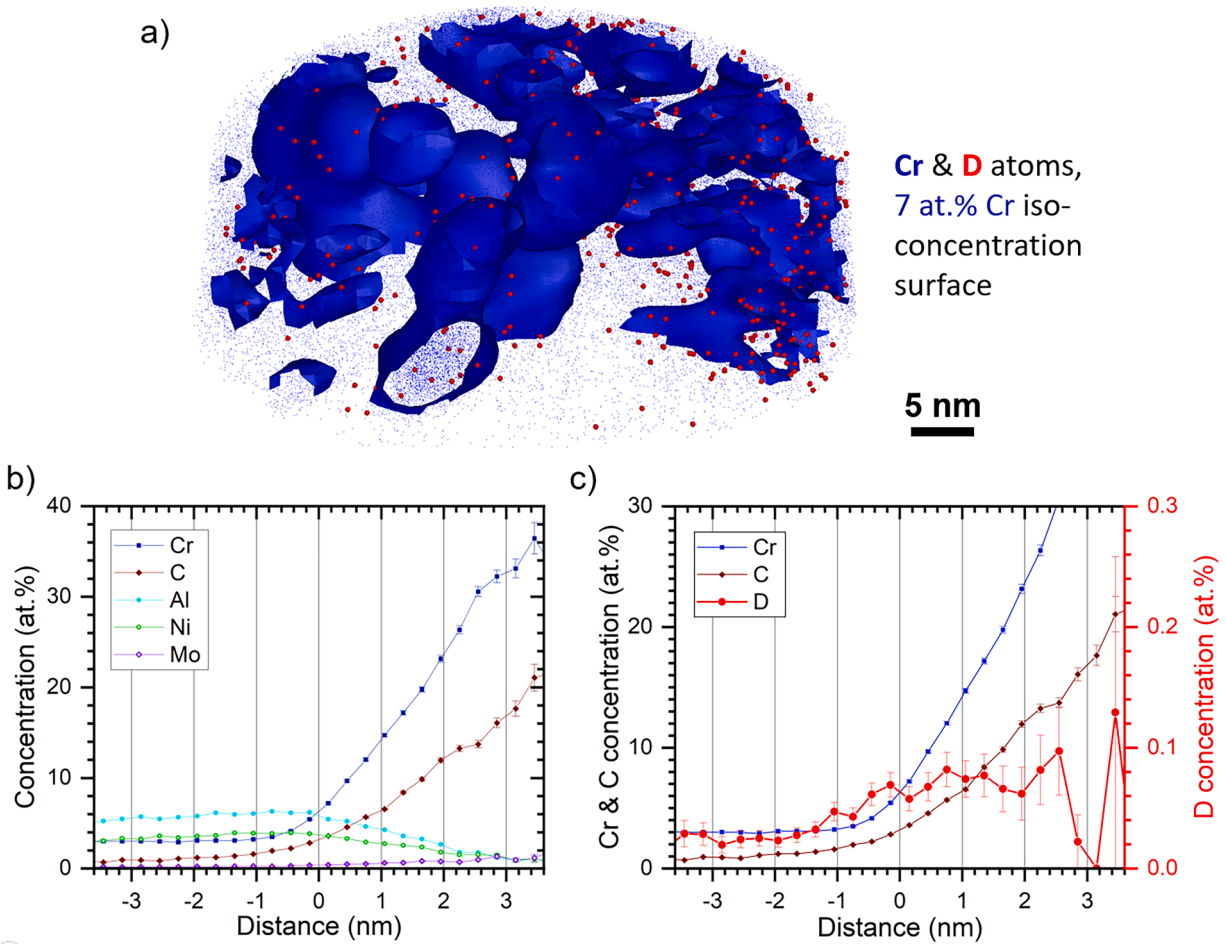

Fig. 3. (a) APT reconstruction of the charged specimen; Cr and D atoms as well as the 7 at.% Cr iso-concentration surfaces are shown. (b) Proxigram of 7 at.% Cr iso-concentration surfaces displaying atomic concentrations near and within the Cr-carbides; (c) Depiction of Cr, C and D concentration as a function of distance to the iso-concentration surface.

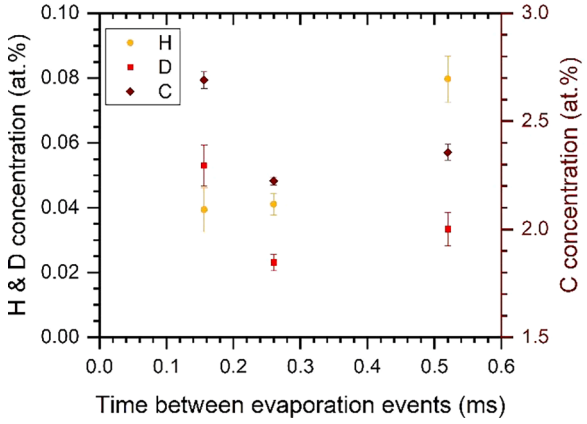

Fig. 4. Concentrations of H, D as well as C as a function of the time between evaporation events (calculated from the pulse frequency and the detection rate) during APT measurement.

content, i.e., in regions where more carbides are present.

During APT measurements of steel in voltage mode, as opposed to laser mode, the evaporation of H_2^+ ions is inhibited. The variation in pulse frequency, together with the absence of a 2 Da peak for the uncharged specimen, validates the assumption that the peak at 2 Da in the mass spectrum is indeed D^+ and not H_2^+.

The Hybrid model alloy in this study is precipitation strengthened by intermetallic ß-NiAl as well as carbides. The ß-NiAl particles are coherent and have a small misfit [42]. Therefore, it is not expected that they provide significant H trapping sites. The alloy has only Cr (except for a limited amount of Mo) as carbide forming element. In this way, the trapping capability of Cr-carbides is investigated without interference from other carbide types.

Since the size of the carbides in this material is in the same range as the lateral resolution of concentration gradients, the interface of precipitates cannot be unambiguously distinguished from the interior of the particles. However, the fact that D is already present at the beginning of the C and Cr gradient in the vicinity of the precipitates suggests that the interface is the more prominent trapping site. This is supported by microautoradiography [43] as well as time-of-flight secondary ion mass spectrometry [44]. TDMS of lab-cast Fe-C-Cr alloy suggests the interface as trapping site by comparing the measured H content to the available interface area of differently sized $Cr_{23}C_6$ precipitates [45]. Looking at different carbides, it was shown that D resides within VC precipitates by APT with fast cooling after charging [13,14]. The fact that trapping sites are within the carbides is supported by neutron scattering [46]. It is known that VC has a high tolerance for C vacancies, thus offering possible trapping sites for H [47]. In contrast, NbC seems to trap H at the interfaces as documented by the same methods [15,48].

TDMS is a commonly used method to measure the de-trapping activation energy for H of microstructural features in a material. However, the desorption peak shape and temperature is dependent on the charging method as well as the initial H distribution [49,50]. We performed 24 h charging on the TDMS samples to ensure saturation and a homogeneous

distribution of H through the samples thickness. This was further enhanced by degassing for 24 h at 50 °C. Considering the temperatures of the H desorption peaks for the three heating rates, a trapping energy of 15.6 kJ/mol was measured, as illustrated in Fig. 5(a). This is in good agreement with trapping energies of various carbides in martensitic steel investigated in a similar manner by Lee et al. [51].

The peak shape in our study as well as in [51] suggests that there is remaining H in the samples. We therefore performed further degassing for 72 h and 168 h (see Fig. 5(b)). The peak shape in the TDMS curve after 168 h degassing suggests that there is more than one trap. Hence, deconvolution was performed and trap energies of 45.5 and 56 kJ/mol were measured, as shown in Fig. 5(c). This is comparable with trapping energies for interfaces of $Cr_{23}C_6$ precipitates, reported to be 49 to 55 kJ/mol for 50 to 100 nm sized precipitates [45] as well as 44.4 kJ/mol for $Cr_{23}C_6$ with sizes of about 1 μm [44]. These values are higher than 21.5 kJ/mol, reported for coherent Mo_2C carbides [10]. Values reported for VC range from 33–35 kJ/mol [9] to 52–67 kJ/mol [52]. In studies regarding TiC the character of the interface is discussed extensively [38, 53]. Semi-coherent TiC interfaces are prominent trapping sites with de-trapping energies of 46 to 59 kJ/mol, whereas the incoherent TiC interfaces are considered irreversible traps for H with de-trapping energies larger than 68 kJ/mol [38].

So far, the use of cryogenic transfer was thought to be necessary. Takahashi et al. [12] report on unsuccessful cathodic charging of nano-sized TiC containing steel. After a transfer time of 20 min at RT, D could not be observed with certainty. They moved on to a gas charging cell with fast cooling capability. TiC has been reported to have a high saddle energy around the trapping sites [37]. It could be that electrochemical charging was not suitable to overcome this saddle energy. Breen et al. investigated different workflows to measure H/D in pearlitic wire [22]. They found a weak D signal at cementite interfacial regions in some of their RT samples after 1 h electrolytic charging at -1.2 V, however, no D was measured after 5 min of charging. The duration of RT-transfer was not reported, and the highest D concentration was measured after cryogenic transfer.

The findings in this work therefore suggest that nano-scale Cr-carbides act as strong H traps that can retain H/D for an extended period of time. To optimize the H trapping capability, the positions of trapping sites are important. Trapping inside the carbides would require a large volume fraction in the microstructure. However, since the D concentration is elevated at the interfaces, a large number density of nm-sized carbides offers abundant trapping sites. This leads to a significant trapping capacity for H, as can be seen by the amount of desorbed H in Fig. 5(d), and therefore most likely also resilience to HE. The investigated microstructure in this study is a promising step forward to produce HE resistant steel with lean alloying design.

In this work, we showed that D can be trapped in the vicinity of nano-scale Cr-carbides in a co-precipitation model alloy. The measurement in voltage mode prevents the formation of H_2^+ ions overlapping with D^+. Furthermore, the evaporation rate method demonstrated by Meier et al.

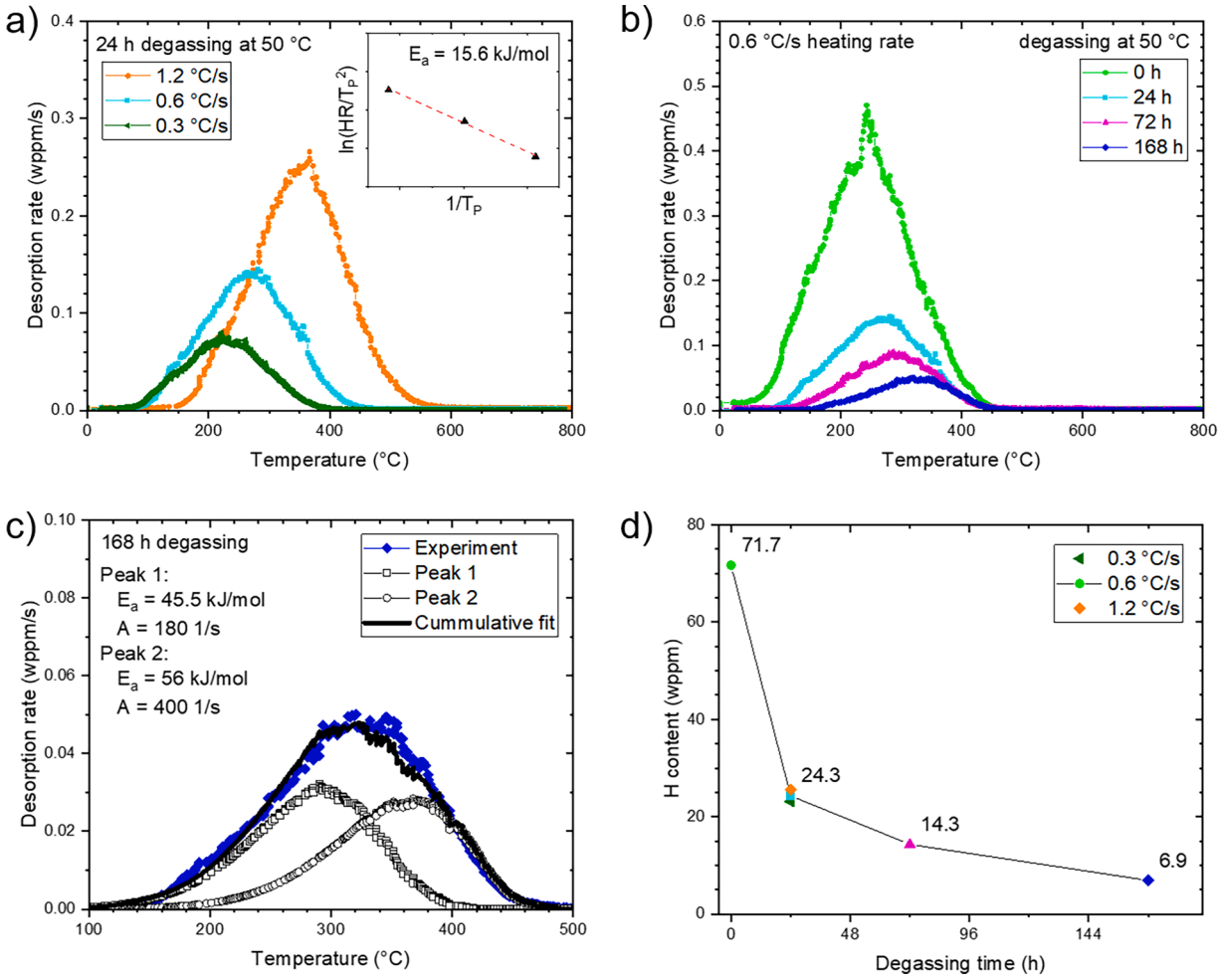

Fig. 5. (a) TDMS measurements with different heating rates after 24 h of degassing at 50 °C. The inset shows the activation energy (E_a) calculated from peak temperatures (T_P) and heating rates (HR). (b) Desorption curves with the same heating rate after different degassing times. (c) Deconvoluted TDMS spectrum after 168 h of degassing to two H peaks with different de-trapping activation energies. (d) Total amount of H in wppm evaluated under the desorption curves as a function of degassing time. Labels indicate the values for measurements with 0.6 °C/s heating rate.

[41] was employed and could confirm that the presence of D is not related to measurement parameters. The amount of D is rather correlated to C. We show that D is trapped already in the vicinity of Cr-carbides suggesting the interface as the major trapping site. No D is located in connection to the intermetallic ß-NiAl. The remaining traps after 168 h of degassing at 50 °C have trapping energies of 45.5 and 56 kJ/mol measured by TDMS. Moreover, this work demonstrates that strong H trapping sites can be measured in APT without cryogenic transfer.

Declaration of Competing Interest

The authors declare that they have no conflict of interest.

Acknowledgements

The model alloy is produced under the Vinnova sponsored project HY-Toolbox (2020-03115). The research is funded by the Swedish Research Council (2021-05072). The APT and TEM measurements were performed at Chalmers Materials Analysis Laboratory (CMAL). The TDMS measurements were performed at Swerim AB.

Supplementary materials

Supplementary material associated with this article can be found, in the online version, at doi:10.1016/j.scriptamat.2023.115963.

References

[1] S. Lynch, Hydrogen embrittlement phenomena and mechanisms, Corros. Rev. 30 (2012) 105–123, https://doi.org/10.1515/corrrev-2012-0502.
[2] Z. Sun, C.H. Liebscher, S. Huang, Z. Teng, G. Song, G. Wang, M. Asta, M. Rawlings, M.E. Fine, P.K. Liaw, New design aspects of creep-resistant NiAl-strengthened ferritic alloys, Scr. Mater. 68 (2013) 384–388, https://doi.org/10.1016/J.SCRIPTAMAT.2012.10.040.
[3] J. Venezuela, Q. Zhou, Q. Liu, H. Li, M. Zhang, M.S. Dargusch, A. Atrens, The influence of microstructure on the hydrogen embrittlement susceptibility of martensitic advanced high strength steels, Mater. Today Commun. 17 (2018) 1–14, https://doi.org/10.1016/J.MTCOMM.2018.07.011.
[4] W.H. Johnson, On some remarkable changes produced in iron and steel by the action of hydrogen and acids, R. Soc. 23 (1875) 168–179.
[5] T.I. Ramjaun, S.W. Ooi, R. Morana, H.K.D.H. Bhadeshia, Designing steel to resist hydrogen embrittlement: part 1–trapping capacity, Mater. Sci. Technol. 34 (2018) 1737–1746, https://doi.org/10.1080/02670836.2018.1475919.
[6] H.K.D.H. Bhadeshia, Prevention of hydrogen embrittlement in steels, ISIJ Int. 56 (2016) 24–36, https://doi.org/10.2355/isijinternational.ISIJINT-2015-430.
[7] H.G. Lee, J.Y. Lee, Hydrogen trapping by TiC particles in iron, Acta Metall. 32 (1984) 131–136, https://doi.org/10.1016/0001-6160(84)90210-4.
[8] C. Zhang, Y. Liu, C. Jiang, J. Xiao, Effects of niobium and vanadium on hydrogen-induced delayed fracture in high strength spring steel, J. Iron Steel Res. Int. 18 (2011) 49–53, https://doi.org/10.1016/S1006-706X(11)60077-0.
[9] H. Asahi, D. Hirakami, S. Yamasaki, Hydrogen trapping behavior in vanadium-added steel, ISIJ Int. 43 (2003) 527–533, https://doi.org/10.2355/isijinternational.43.527.
[10] D. Li, R.P. Gangloff, J.R. Scully, Hydrogen Trap states in ultrahigh-strength AERMET 100 steel, Metall. Mater. Trans. A Phys. Metall. Mater. Sci. 35 A (2004) 849–864, https://doi.org/10.1007/s11661-004-0011-1.
[11] Y.C. Lin, I.E. McCarroll, Y.T. Lin, W.C. Chung, J.M. Cairney, H.W. Yen, Hydrogen trapping and desorption of dual precipitates in tempered low-carbon martensitic steel, Acta Mater. 196 (2020) 516–527, https://doi.org/10.1016/j.actamat.2020.06.046.
[12] J. Takahashi, K. Kawakami, Y. Kobayashi, T. Tarui, The first direct observation of hydrogen trapping sites in TiC precipitation-hardening steel through atom probe tomography, Scr. Mater. 63 (2010) 261–264, https://doi.org/10.1016/j.scriptamat.2010.03.012.
[13] J. Takahashi, K. Kawakami, T. Tarui, Direct observation of hydrogen-trapping sites in vanadium carbide precipitation steel by atom probe tomography, Scr. Mater. 67 (2012) 213–216, https://doi.org/10.1016/j.scriptamat.2012.04.022.
[14] Y.S. Chen, D. Haley, S.S.A. Gerstl, A.J. London, F. Sweeney, R.A. Wepf, W. M. Rainforth, P.A.J. Bagot, M.P. Moody, Direct observation of individual hydrogen atoms at trapping sites in a ferritic steel, Science 355 (80) (2017) 1196–1199, https://doi.org/10.1126/science.aal2418.
[15] Y.S. Chen, H. Lu, J. Liang, A. Rosenthal, H. Liu, G. Sneddon, I. McCarroll, Z. Zhao, W. Li, A. Guo, J.M. Cairney, Observation of hydrogen trapping at dislocations, grain boundaries, and precipitates, Science 367 (80) (2020) 171–175, https://doi.org/10.1126/science.aaz0122.
[16] W. Lefebvre-Ulrikson, F. Vurpillot, X. Sauvage (Eds.), Atom Probe Tomography: Put Theory Into Practice, Academic Press, London, 2016.
[17] G. Sundell, M. Thuvander, H.O. Andrén, Hydrogen analysis in APT: methods to control adsorption and dissociation of H2, Ultramicroscopy 132 (2013) 285–289, https://doi.org/10.1016/j.ultramic.2013.01.007.
[18] Y. Hayashi, H. Hagi, A. Tahara, Diffusion coefficients of hydrogen and deuterium in iron determined by permeation with gas, ion and electrochemical charging, Zeitschrift Fur Phys. Chem. 164 (1989) 815–820, https://doi.org/10.1524/zpch.1989.164.Part_1.0815.
[19] W. Raczynski, Permeability, Diffusivity, and Solubility of Hydrogen and Deuterium in Pure Iron at 10 to 60 C, Phys. Status Solid. 48 (1978) K27–K30, https://doi.org/10.1002/pssa.2210480143.
[20] H. Takamizawa, K. Hoshi, Y. Shimizu, F. Yano, K. Inoue, S. Nagata, T. Shikama, Y. Nagai, Three-dimensional characterization of deuterium implanted in silicon using atom probe tomography, Appl. Phys. Express. 6 (2013), https://doi.org/10.7567/APEX.6.066602.
[21] D. Haley, S.V. Merzlikin, P. Choi, D. Raabe, Atom probe tomography observation of hydrogen in high-Mn steel and silver charged via an electrolytic route, Int. J. Hydrogen Energy 39 (2014) 12221–12229, https://doi.org/10.1016/j.ijhydene.2014.05.169.
[22] A.J. Breen, L.T. Stephenson, B. Sun, Y. Li, O. Kasian, D. Raabe, M. Herbig, B. Gault, Solute hydrogen and deuterium observed at the near atomic scale in high-strength steel, Acta Mater. 188 (2020) 108–120, https://doi.org/10.1016/j.actamat.2020.02.004.
[23] I.E. McCarroll, Y.C. Lin, A. Rosenthal, H.W. Yen, J.M. Cairney, Hydrogen trapping at dislocations, carbides, copper precipitates and grain boundaries in a dual precipitating low-carbon martensitic steel, Scr. Mater. 221 (2022) 114934, https://doi.org/10.1016/j.scriptamat.2022.114934.
[24] L.T. Stephenson, A. Szczepaniak, I. Mouton, K.A.K. Rusitzka, A.J. Breen, U. Tezins, A. Sturm, D. Vogel, Y. Chang, P. Kontis, A. Rosenthal, J.D. Shepard, U. Maier, T.F. Kelly, D. Raabe, B. Gault, The Laplace project: an integrated suite for correlative atom probe tomography and electron microscopy under cryogenic and UHV conditions, (2018) 1–13. http://arxiv.org/abs/1805.10836.
[25] J.M. Cairney, I. McCarroll, Y.S. Chen, K. Eder, T. Sato, Z. Liu, A. Rosenthal, R. Wepf, Correlative UHV-Cryo Transfer Suite, Connecting atom probe, SEM-FIB, Transmission electron microscopy via an environmentally-controlled glovebox, Microsc. Microanal. 25 (2019) 2494–2495, https://doi.org/10.1017/s1431927619013205.
[26] I.E. McCarroll, P.A.J. Bagot, A. Devaraj, D.E. Perea, J.M. Cairney, New frontiers in atom probe tomography: a review of research enabled by cryo and/or vacuum transfer systems, Mater. Today Adv. 7 (2020) 100090, https://doi.org/10.1016/j.mtadv.2020.100090.
[27] Z.B. Jiao, J.H. Luan, M.K. Miller, Y.W. Chung, C.T. Liu, Co-precipitation of nanoscale particles in steels with ultra-high strength for a new era, Mater. Today 20 (2017) 142–154, https://doi.org/10.1016/J.MATTOD.2016.07.002.
[28] H.J. Kong, C.T. Liu, A Review On Nano-Scale Precipitation In Steels, Technologies 6 (2018) 36, https://doi.org/10.3390/TECHNOLOGIES6010036.
[29] Z. Xiong, I. Timokhina, E. Pereloma, Clustering, nano-scale precipitation and strengthening of steels, Prog. Mater. Sci. 118 (2021) 100764, https://doi.org/10.1016/J.PMATSCI.2020.100764.
[30] J.E. Andersson, F. Lindberg, P. Ölund, Hybrid steel enhances component performance at reduced weight, Light. Des. Worldw. 12 (2019) 34–39, https://doi.org/10.1007/s41777-018-0063-3.
[31] J.E. Andersson, F. Lindberg, S. Ooi, Hybrid steel and its potential for bearing applications. ASTM Special Technical Publication, ASTM International, 2020, pp. 436–454, https://doi.org/10.1520/STP162320190163.
[32] H. Zhao, B. Gault, D. Ponge, D. Raabe, F. De Geuser, Parameter free quantitative analysis of atom probe data by correlation functions: application to the precipitation in Al-Zn-Mg-Cu, Scr. Mater. 154 (2018) 106–110, https://doi.org/10.1016/j.scriptamat.2018.05.024.
[33] F. De Geuser, W. Lefebvre, F. De Geuser, W. Lefebvre, Determination of matrix composition based on solute-solute nearest-neighbor distances in atom probe tomography, Microsc. Res. Tech. 74 (2011) 257–263, https://doi.org/10.1002/jemt.20899.
[34] F. Vurpillot, A. Bostel, D. Blavette, Trajectory overlaps and local magnification in three-dimensional atom probe, Appl. Phys. Lett. 76 (2000) 3127–3129, https://doi.org/10.1063/1.126545.
[35] D.J. Larson, B. Gault, B.P. Geiser, F. De Geuser, F. Vurpillot, Atom probe tomography spatial reconstruction: status and directions, Curr. Opin. Solid State Mater. Sci. 17 (2013) 236–247, https://doi.org/10.1016/j.cossms.2013.09.002.
[36] H.E. Kissinger, Reaction kinetics in differential thermal analysis, Anal. Chem 29 (1957) 1702–1706, https://doi.org/10.1021/ac60131a045.
[37] J.Y. Lee, S.M. Lee, Hydrogen trapping phenomena in metals with B.C.C. and F.C.C. crystals structures by the desorption thermal analysis technique, Surf. Coatings Technol. 28 (1986) 301–314, https://doi.org/10.1016/0257-8972(86)90087-3.
[38] F.G. Wei, T. Hara, K. Tsuzaki, Precise determination of the activation energy for desorption of hydrogen in two Ti-added steels by a single thermal-desorption spectrum, Metall. Mater. Trans. B Process Metall. Mater. Process. Sci. 35 (2004) 587–597, https://doi.org/10.1007/s11663-004-0057-x.
[39] Z. Guo, W. Sha, D. Vaumousse, Microstructural evolution in a PH13-8 stainless steel after ageing, Acta Mater. 51 (2003) 101–116, https://doi.org/10.1016/S1359-6454(02)00353-1.
[40] M. Thuvander, J. Weidow, J. Angseryd, L.K.L. Falk, F. Liu, M. Sonestedt, K. Stiller, H.O. Andrén, Quantitative atom probe analysis of carbides, Ultramicroscopy 111 (2011) 604–608, https://doi.org/10.1016/J.ULTRAMIC.2010.12.024.

[41] M.S. Meier, M.E. Jones, P.J. Felfer, M.P. Moody, D. Haley, Extending estimating hydrogen content in atom probe tomography experiments where H 2 molecule formation occurs, Microsc. Microanal. 28 (2022) 1231–1244, https://doi.org/10.1017/S1431927621012332.
[42] L.M. Pike, I.M. Anderson, C.T. Liu, Y.A. Chang, Site occupancies, point defect concentrations, and solid solution hardening in B2 (Ni,Fe)Al, Acta Mater 50 (2002) 3859–3879, https://doi.org/10.1016/S1359-6454(02)00192-1.
[43] C. Paes de Oliveira, M. Aucouturier, P. Lacombe, Hydrogen trapping in BCC Fe-Cr Alloys (7 ~ 9. 4 Wt% Cr) as studied by microautoradiography-contribution of carbon-hydrogen interaction-consequences on hydrogen cracking, Corrosion 36 (1980) 53–59, https://doi.org/10.5006/0010-9312-36.2.53.
[44] T. Wang, X. Fang, H. Zhang, W. Lv, J. Ma, W. Liang, L. Zheng, Observation of hydrogen trap and hydrogen embrittlement of 430 ferritic stainless steel, Mater. Lett. 313 (2022) 131728, https://doi.org/10.1016/j.matlet.2022.131728.
[45] T. Depover, K. Verbeken, Hydrogen trapping and hydrogen induced mechanical degradation in lab cast Fe-C-Cr alloys, Mater. Sci. Eng. A. 669 (2016) 134–149, https://doi.org/10.1016/j.msea.2016.05.018.
[46] B. Malard, B. Remy, C. Scott, A. Deschamps, J. Chêne, T. Dieudonné, M.H. Mathon, Hydrogen trapping by VC precipitates and structural defects in a high strength Fe-Mn-C steel studied by small-angle neutron scattering, Mater. Sci. Eng. A. 536 (2012) 110–116, https://doi.org/10.1016/j.msea.2011.12.080.
[47] J. Takahashi, K. Kawakami, Y. Kobayashi, Origin of hydrogen trapping site in vanadium carbide precipitation strengthening steel, Acta Mater. 153 (2018) 193–204, https://doi.org/10.1016/J.ACTAMAT.2018.05.003.
[48] M. Ohnuma, J. ichi Suzuki, F.G. Wei, K. Tsuzaki, Direct observation of hydrogen trapped by NbC in steel using small-angle neutron scattering, Scr. Mater. 58 (2008) 142–145, https://doi.org/10.1016/j.scriptamat.2007.09.026.
[49] M. Enomoto, L. Cheng, H. Mizuno, Y. Watanabe, T. Omura, J. Sakai, K. Yokoyama, H. Suzuki, R. Okuma, Hydrogen Absorption into austenitic stainless steels under high-pressure gaseous hydrogen and cathodic charge in aqueous solution, Metall. Mater. Trans. E. 1 (2014) 331–340, https://doi.org/10.1007/s40553-014-0034-5.
[50] E. Wallaert, T. Depover, M. Arafin, K. Verbeken, Thermal desorption spectroscopy evaluation of the hydrogen-trapping capacity of NbC and NbN precipitates, Metall. Mater. Trans. A Phys. Metall. Mater. Sci. 45 (2014) 2412–2420, https://doi.org/10.1007/s11661-013-2181-1.
[51] J. Lee, T. Lee, D.J. Mun, C.M. Bae, C.S. Lee, Comparative study on the effects of Cr, V, and Mo carbides for hydrogen-embrittlement resistance of tempered martensitic steel, Sci. Rep. 9 (2019) 1–9, https://doi.org/10.1038/s41598-019-41436-2.
[52] T. Depover, K. Verbeken, Evaluation of the effect of V4C3 precipitates on the hydrogen induced mechanical degradation in Fe-C-V alloys, Mater. Sci. Eng. A. 675 (2016) 299–313, https://doi.org/10.1016/j.msea.2016.08.053.
[53] F.G. Wei, K. Tsuzaki, Quantitative analysis on hydrogen trapping of TiC particles in steel, Metall. Mater. Trans. A Phys. Metall. Mater. Sci. 37 (2006) 331–353, https://doi.org/10.1007/S11661-006-0004-3/METRICS.